# Splitting $CO_2$ into CO and $O_2$ by a single catalyst

Zuofeng Chen[a], Javier J. Concepcion[a], M. Kyle Brennaman[a], Peng Kang[a], Michael R. Norris[a], Paul G. Hoertz[b], and Thomas J. Meyer[a,1]

[a]Department of Chemistry, University of North Carolina, Chapel Hill, NC 27599; and [b]RTI International, Research Triangle Park, NC 27709

Edited by Jack Halpern, University of Chicago, Chicago, IL, and approved April 25, 2012 (received for review February 23, 2012)

**The metal complex $[(tpy)(Mebim\text{-}py)Ru^{II}(S)]^{2+}$ (tpy = 2,2′ : 6′,2″-terpyridine; Mebim-py = 3-methyl-1-pyridylbenzimidazol-2-ylidene; S = solvent) is a robust, reactive electrocatalyst toward both water oxidation to oxygen and carbon dioxide reduction to carbon monoxide. Here we describe its use as a single electrocatalyst for $CO_2$ splitting, $CO_2 \rightarrow CO + 1/2\,O_2$, in a two-compartment electrochemical cell.**

artificial photosynthesis | polypyridyl Ru complexes | proton coupled electron transfer | single-site catalysis | solar fuels

Rising energy prices, diminishing reserves of petroleum, and environmental concerns are driving new thinking about our energy future. Given its availability, with approximately 10,000 times the daily energy input required to meet current energy consumption, solar energy could be the ultimate answer. However, solar energy is diffuse, spread over the earth's surface, and requires vast collection areas for large-scale applications (1). A more difficult challenge is the intermittency of the sun as an energy source. Meeting the challenge of providing power at night will require energy storage on massive scales at levels exceeding the ability of existing or foreseeable energy storage technologies (2, 3). The only realistic alternative is energy storage in chemical bonds and the increasingly popular concept of "solar fuels." Solar fuels mimic natural photosynthesis in using solar energy and artificial photosynthesis to convert readily available sources, water and carbon dioxide, into high-energy fuels. Target reactions include water splitting into hydrogen and oxygen and reduction of carbon dioxide to carbon monoxide, other oxygenates, or hydrocarbons (Eqs. **1–3**), as follows:

$$2H_2O + 4h\nu \rightarrow O_2 + 2H_2 \quad [1]$$

$$2CO_2 + 4h\nu \rightarrow 2CO + O_2 \quad [2]$$

$$2H_2O + CO_2 + 8h\nu \rightarrow 2O_2 + CH_4. \quad [3]$$

Carrying out these reactions presents a major challenge in chemical reactivity given their multiphoton, multielectron, multiatom character. It is reassuring that similar hurdles have been overcome in natural photosynthesis, in which light-driven reduction of $CO_2$ to carbohydrates by water occurs (Eq. **4**). However, photosynthesis in green plants took 2–3 billion years to evolve and utilizes a complex architecture that utilizes thousands and thousands of atoms and multiple integrated assemblies (4, 5).

$$6H_2O + 6CO_2 \rightarrow C_6H_{12}O_6 + 6O_2 \quad (\Delta G^\circ = 29.1\ \text{eV}, \quad \text{or} \quad 2820\ \text{kJ/mol}) \quad [4]$$

A simplifying factor, suggesting a mechanistic approach, comes with recognition that the target energy storage reactions can be split into constituent "half reactions" which are shown for $CO_2$ splitting in Eqs. **5** and **6**. Photosynthesis in green plants occurs in the thylakoid membrane and uses physically separated molecular assemblies for light-driven water oxidation (Photosystem II) and $CO_2$ reduction (Photosystem I and the Calvin cycle) (6, 7). Electron/proton equilibration occurs by intra- or transmembrane electron/proton transfer channels driven by free energy gradients.

Application of a "half-reaction" strategy in artificial photosynthesis poses similar challenges. In both water oxidation and $CO_2$ reduction, mechanisms involving one-electron reactions are energetically untenable. They result in $^\bullet OH$ on oxidation or $CO_2^{\bullet-}$ on reduction at potentials too high to be of interest in solar fuels half-reaction with $E^\circ = 2.72$ V vs. NHE ($E^\circ$ is the standard electrode potential) for the $^\bullet OH + H^+ + e^- \rightarrow H_2O$ couple and $E^\circ = -1.90$ V for the $CO_2 + e^- \rightarrow CO_2^{\bullet-}$ couple. By comparison, $E^\circ = 1.23$ V for water oxidation to oxygen in Eq. **5** and $E^\circ = -0.12$ V for $CO_2$ reduction to CO in Eq. **6**. The energy available in a 500-nm photon in the visible region of the solar spectrum is 2.48 eV. For the reaction, $H_2O + CO_2 \rightarrow {}^\bullet OH + H^+ + CO_2^{\bullet-}$, $E^\circ = -4.62$ V ($\Delta G^\circ = +4.62$ eV) and, for the $CO_2$ splitting reaction in Eq. **7**, $E^\circ = -1.35$ V ($\Delta G^\circ = +2.70$ eV). The CO product in Eq. **7** is of interest as a component of syngas, a hydrogen/CO mixture for methanol synthesis (8, 9).

$$O_2 + 4H^+ + 4e^- \rightarrow 2H_2O \quad (E^\circ = 1.23\ \text{V vs. NHE}) \quad [5]$$

$$CO_2 + 2H^+ + 2e^- \rightarrow CO + H_2O \quad (E^\circ = -0.12\ \text{V vs. NHE}) \quad [6]$$

$$CO_2 \rightarrow CO + \frac{1}{2}O_2 \quad [7]$$

In order to carry out these reactions at or near the thermodynamic potentials for the separate half reactions requires catalysis and utilization of multielectron, multiproton transfer catalysis. This, in turn, requires the accumulation of multiple redox equivalents at single chemical sites or clusters and mechanistic pathways that avoid high-energy, $1e^-$ intermediates. A key element in both is proton coupled electron transfer (PCET) and use of half reactions in which both protons and electrons are lost or gained to avoid charge buildup. A second is electron-proton transfer (EPT), in which concerted electron-proton transfer occurs to avoid high-energy intermediates (10–12).

Impressive advances have been made in catalytic water oxidation by transition metal complexes at single-site catalysts (13–25). Progress has also been made on catalytic reduction of $CO_2$ to CO (26–36). Both present a formidable challenge in chemical reactivity. Nonetheless, we report here that a single metal complex catalyst suffices for both half reactions and apply it for electrocatalytic $CO_2$ splitting.

Among the family of single-site Ru complex catalysts for water oxidation, $[(tpy)(Mebim\text{-}py)Ru^{II}(S)]^{2+}$ **1** (tpy = 2, 2′ : 6′, 2″-terpyridine; Mebim-py = 3-methyl-1-pyridylbenzimidazol-2-ylidene; S = solvent. As $[(tpy)(Mebim\text{-}py)Ru^{II}(OH_2)]^{2+}$ in water) is a robust example. It undergoes water oxidation by the mechan-

Author contributions: Z.C. and T.J.M. designed research; Z.C. performed research; J.J.C., M.K.B., P.K., M.R.N., and P.G.H. contributed new reagents/analytic tools; Z.C. and T.J.M. analyzed data; and Z.C. and T.J.M. wrote the paper.

The authors declare no conflict of interest.

This article is a PNAS Direct Submission.

[1]To whom correspondence should be addressed. E-mail: tjmeyer@unc.edu.

This article contains supporting information online at www.pnas.org/lookup/suppl/doi:10.1073/pnas.1203122109/-/DCSupplemental.

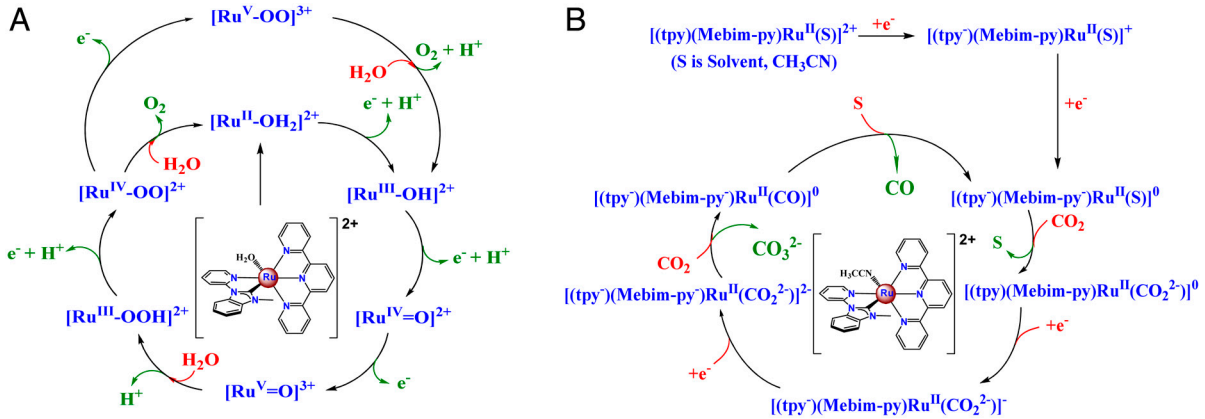


**Scheme 1.** (*A*) Mechanism for electrocatalytic single-site water oxidation by **1** as $[(tpy)(Mebim\text{-}py)Ru^{II}(OH_2)]^{2+}$ in water (21, 25). (*B*) Mechanism for electrocatalytic reduction of $CO_2$ to CO by **1** as $[(tpy)(Mebim\text{-}py)Ru^{II}(NCCH_3)]^{2+}$ in $CH_3CN$ (36).

ism shown in Scheme 1*A* (21, 25). In this mechanism, stepwise PCET oxidation and proton loss from $Ru^{II}\text{-}OH_2{}^{2+}$ provide access to $Ru^{V}=O^{3+}$. This high-oxidation state intermediate undergoes O-atom attack on water to give $Ru^{III}\text{-}OOH^{2+}$. Once formed, the peroxide intermediate undergoes further oxidation and $O_2$ loss and reenters the catalytic cycle as $Ru^{III}\text{-}OH^{2+}$. An important factor in the enhanced reactivity of the carbene complex compared to related complexes comes from the favorable driving force for the O—O bond forming step (24, 25).

Electrocatalyzed reduction of $CO_2$ by transition metal complexes, including polypyridyl complexes of Ru, is also well-known (26–36). Mechanistic insight has come from electrochemical and spectroscopic monitoring. A key element for polypyridyl catalysts is initial polypyridyl-based reduction with the reduced ligands acting as electron reservoirs for subsequent $CO_2$ reduction at the metal. For example, in Scheme 1*B* (36), **1** (as $[(tpy)(Mebim\text{-}py)Ru^{II}(NCCH_3)]^{2+}$) is also a $CO_2$ reduction catalyst in $CH_3CN$. It undergoes two sequential $1e^-$ ligand-based reductions at $E_{p,c} = -1.07$ V and $-1.33$ V vs. NHE ($E_{p,c}$ is the reductive peak potential) to give $[(tpy^-)(Mebim\text{-}py^-)Ru^{II}(NCCH_3)]^0$. Ligand-based reduction is followed by rate limiting $CO_2$ coordination, $[(tpy^-)(Mebim\text{-}py^-)Ru^{II}(NCCH_3)]^0 + CO_2 \rightarrow [(tpy)(Mebim\text{-}py)Ru^{II}(CO_2{}^{2-})]^0 + CH_3CN$. Once the metallocarboxylate intermediate is formed, it undergoes further reduction at the ligands to give CO and $CO_3{}^{2-}$ (Eq. **8**) as final products (36).

$$2CO_2 + 2e^- \xrightarrow{[(tpy)(Mebim\text{-}py)Ru^{II}(NCCH_3)]^{2+}} CO + CO_3{}^{2-} \qquad [8]$$

Water oxidation and $CO_2$ reduction by **1** in $CH_3CN\text{-}H_2O$ mixtures were investigated. In the Ru(II) state, with 10% added $CH_3CN$ (vol/vol), in 0.1 M $NaH_2PO_4/Na_2HPO_4$ buffer (pH 7.45), aqua substitution by acetonitrile, $Ru^{II}\text{-}OH_2{}^{2+} + CH_3CN \rightarrow Ru^{II}\text{-}NCCH_3{}^{2+} + H_2O$, occurs and was complete in 10 min. This was shown by spectrophotometric monitoring, and the shift in $\lambda_{max}$ for the dominant metal-to-ligand charge

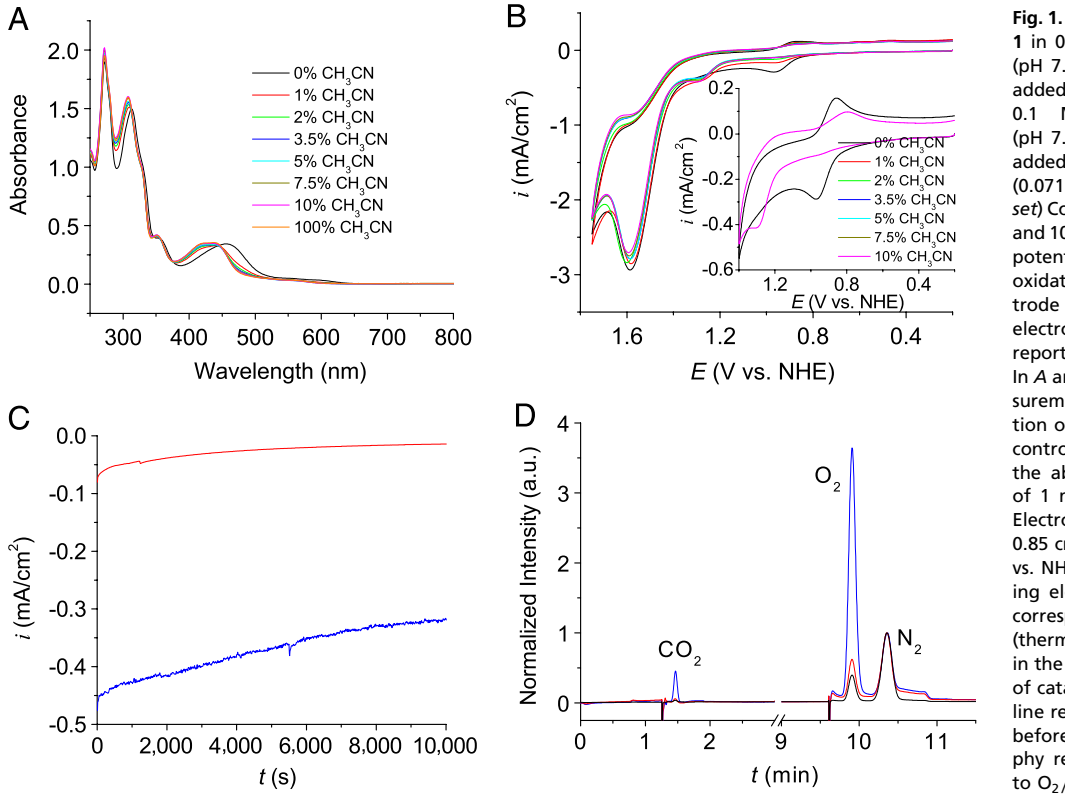


**Fig. 1.** (*A*) UV–visible spectra of 50 μM **1** in 0.1 M $NaH_2PO_4/Na_2HPO_4$ buffer (pH 7.45) with increasing amounts of added $CH_3CN$. (*B*) CVs of 1 mM **1** in 0.1 M $NaH_2PO_4/Na_2HPO_4$ buffer (pH 7.45) with increasing amounts of added $CH_3CN$. Electrode, glassy carbon (0.071 $cm^2$); scan rate, 100 mV/s. (*Inset*) Comparison of CVs with 0% (black) and 10% (magenta) added $CH_3CN$ with potential scan reversal before water oxidation wave. The reference electrode used was the saturated calomel electrode (SCE) (0.244 V vs. NHE) with reported potentials converted to NHE. In *A* and *B*, the UV-visible and CV measurements were conducted after addition of $CH_3CN$ for 10 min. (*C*) As in *B*, controlled potential electrolysis in the absence (red) or presence (blue) of 1 mM **1** with 10% added $CH_3CN$. Electrode, BDD|Si (approximately 0.85 $cm^2$); applied potential, 1.55 V vs. NHE. The solution was stirred during electrolysis. (*D*) As in *C*, showing corresponding gas chromatograms (thermal-conductivity detector, TCD) in the absence (red) or presence (blue) of catalyst after electrolysis. The black line represents the gas chromatogram before electrolysis. The chromatography response for $O_2$ was normalized to $O_2/N_2$ in air.

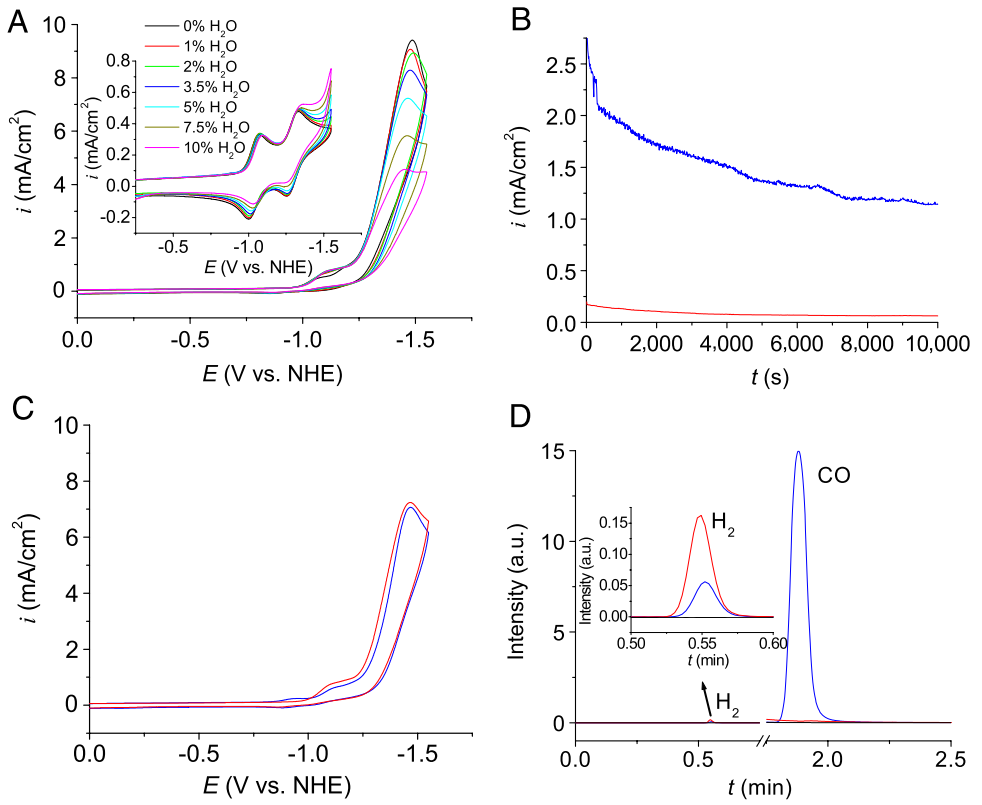


**Fig. 2.** (*A*) CVs of 1 mM **1** in 0.1 M $^{n}Bu_4NPF_6/CH_3CN$ under $CO_2$ with increasing amounts of added water. Electrode, glassy carbon (0.071 $cm^2$); scan rate, 100 mV/s. (*Inset*) As in the figure but under Ar. The reference electrode used was $Ag/AgNO_3$ (0.55 V vs. NHE) with reported potentials converted to NHE. (*B*) As in *A*, controlled potential electrolysis with 5% added water under Ar (red) and $CO_2$ (blue). Electrode, glassy carbon (0.071 $cm^2$); applied potential, −1.45 V vs. NHE. The solution was stirred during electrolysis. (*C*) As in *B*, CVs before (red) and after (blue) electrolysis under $CO_2$ at freshly polished glassy carbon electrodes. (*D*) As in *B*, showing corresponding gas chromatograms (pulsed discharge helium ionization detector, PDHID) in the absence (red) or presence (blue) of catalyst after electrolysis. The black line represents the gas chromatogram before electrolysis.

transfer (MLCT) absorption from 456 nm to 420–440 nm (Fig. 1*A*). Cyclic voltammetric (CV) measurements reinforce this observation. Addition of 10% $CH_3CN$, in 0.1 M $NaH_2PO_4/Na_2HPO_4$ buffer (pH 7.45), causes the wave for $Ru^{II}$-$OH_2^{2+} \rightarrow Ru^{III}$-$OH^{2+}$ oxidation at $E_{p,a} = 0.96$ V vs. NHE ($E_{p,a}$ is the oxidative peak potential) to diminish with appearance of a new wave at $E_{p,a} = 1.30$ V for $Ru^{II}$-$NCCH_3{}^{2+} \rightarrow Ru^{III}$-$NCCH_3{}^{3+}$ oxidation (Fig. 1*B*). The sense of the substitution is reversed upon oxidation. As shown in the Fig. 1*B*, *Inset*, in reverse scans, a distorted wave for $Ru^{III}$-$OH^{2+} \rightarrow Ru^{II}$-$OH_2{}^{2+}$ reduction appears at $E_{p,c} = 0.80$ V rather than a wave for $Ru^{III}$-$NCCH_3{}^{3+} \rightarrow Ru^{II}$-$NCCH_3{}^{2+}$ reduction. The reactions that occur in this sequence are shown in Eqs. **9**–**11**. Re-aquation at Ru(III) allows the catalyst to enter the catalytic cycle in Scheme 1*A* as $Ru^{III}$-$OH^{2+}$ and water oxidation to proceed without interference from substitution.

In the cycle in Scheme 1*A*, water oxidation is triggered by oxidation of $Ru^{IV} = O^{2+}$ to $Ru^{V} = O^{3+}$ at an onset potential of approximately 1.4 V vs. NHE. Fig. 1*C* shows the results of a controlled potential electrolysis experiment at 1.55 V with 10% added $CH_3CN$ at a polycrystalline silicon wafer coated with boron-doped diamond (BDD|Si). Electrode choice is important in these experiments with competitive surface oxidation occurring at conventional glassy carbon or other carbon electrodes. The catalytic current decreased initially, but was relatively stable over the 3 h electrolysis period. The current decrease appears to be due to slow catalyst decomposition by oxidation of the carbene ligand.* Analysis of the head space in the electrolysis cell by gas chromatography (Varian 450-GC) demonstrated oxygen production with a Faradaic efficiency of approximately 88% through approximately 5 catalyst turnovers (Fig. 1*D*).

*A small amount of $CO_2$ ($O_2:CO_2 = 20:1$, mol:mol) appeared in the gas chromatographic analysis in Fig. 1*D*, presumably due to slow decomposition of the carbene ligand in the catalyst.

$$[(tpy)(Mebim\text{-}py)Ru^{II}(OH_2)]^{2+} + CH_3CN \rightarrow [(tpy)(Mebim\text{-}py)Ru^{II}(NCCH_3)]^{2+} + H_2O \quad [9]$$

$$[(tpy)(Mebim\text{-}py)Ru^{II}(NCCH_3)]^{2+} - e^- \rightarrow [(tpy)(Mebim\text{-}py)Ru^{III}(NCCH_3)]^{3+} \quad [10]$$

$$[(tpy)(Mebim\text{-}py)Ru^{III}(NCCH_3)]^{3+} + H_2O \rightarrow [(tpy)(Mebim\text{-}py)Ru^{III}(OH)]^{2+} + CH_3CN + H^+ \quad [11]$$

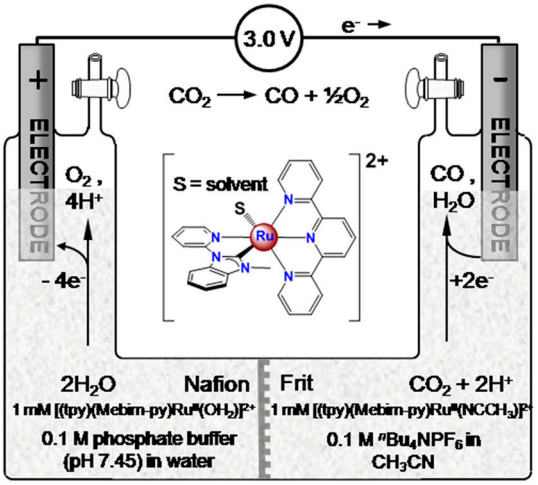


**Fig. 3.** Schematic diagram for the two-compartment, Nafion|Frit-separated electrochemical cell for $CO_2$ splitting. A three-electrode potentiostat was used to control the two-electrode cell with one electrode as the working electrode and the other acting as both counter and reference electrodes. The *iR* drop across the Nafion|Frit was not compensated.

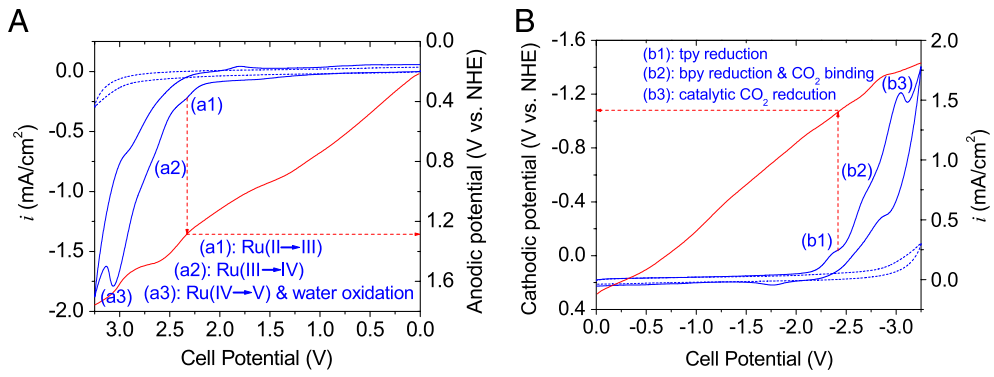


**Fig. 4.** Note Figs. S1 and S2. Blue lines: CVs at glassy carbon electrodes (0.071 $cm^2$) with 10% $CH_3CN$ and 5% $H_2O$ added in the anode and cathode compartments, respectively: (*A*), anodic scan for water oxidation and (*B*), cathodic scan for $CO_2$ reduction. The dashed blue lines are the background without catalyst. Red lines: the applied potential (vs. NHE) at the working electrode during forward potential scans. As examples, the peak potentials for peaks a1 and b1, as determined by the intersecting red dashed lines, are shown in the figure. Scan rate, 100 mV/s.

Fig. 2*A* shows CVs of 1 atm $CO_2$-saturated solutions containing 1 mM **1** in 0.1 M $^nBu_4NPF_6/CH_3CN$ ($^nBu_4N^+$ = tetrabutylammonium cation) at a glassy carbon electrode with addition of increasing amounts of water. Peak currents for electrocatalytic $CO_2$ reduction decreased slightly with added water falling by 20% with 5% added water. Fig. 2*B* shows the results of a controlled potential electrolysis experiment at −1.45 V vs. NHE at a glassy carbon in a $CO_2$ saturated solution with 5% added water. The catalytic current was sustained for at least 3 h with a slow current decrease due to catalyst precipitation on the electrode surface.[†] The catalyst retained its activity as shown by CV measurements at fresh electrodes (Fig. 2*C*). Analysis of the head space in the electrolysis cell by gas chromatography showed formation of CO with a Faradaic efficiency of approximately 85% with 3.5 catalyst turnovers (Fig. 2*D*). A small amount of hydrogen was also detected in the head space with a Faradaic efficiency of <2% (Fig. 2*D*, *Inset*). There was no evidence for $CH_3OH$, HC(O)H, or $HC(O)O^-$ in the liquid phase by gas chromatography (GC-2014, Shimadzu) and $^1H$ NMR (Bruker Avance-400 MHz). The reaction stoichiometry for the half reaction with added water is shown in Eq. **12** (36), as follows:

$$3CO_2 + 2e^- + H_2O \xrightarrow{[(tpy)(Mebim\text{-}py)Ru^{II}(NCCH_3)]^{2+}} CO + 2HCO_3^-. \quad \textbf{[12]}$$

The ability of the single-site Ru carbene complex to act as an electrocatalyst for both water oxidation and $CO_2$ reduction provides a basis for the two compartment electrolysis cell for $CO_2$ splitting shown in Fig. 3. In the cell a Nafion cation exchange membrane cast on a glass frit (Nafion|Frit) was used to separate the compartments (37).[‡]

The *i-E* characteristics of the two-electrode electrochemical cell were examined by CV measurements (Fig. 4). In these experiments, the anode compartment contained the aqueous $NaH_2PO_4/Na_2HPO_4$ buffer (pH 7.45) with 10% added $CH_3CN$ and the cathode 0.1 M $^nBu_4NPF_6$ in $CO_2$-saturated $CH_3CN$ with 5% added $H_2O$. The potential applied at the working electrode was monitored by a second potentiostat (Figs. S1 and S2). Assignment of the current-potential features in Fig. 4 are based on comparisons with profiles for the separate catalytic water oxidation and $CO_2$ reduction half-reactions described here and previously (25, 36).

In the current-potential traces, *i-E* features appear from +2.2 to +3.25 V in Fig. 4*A* and from −2.2 to −3.25 V in Fig. 4*B*. The former are associated with the metal-based oxidations which result in water oxidation in Scheme 1*A*, and the latter to the ligand-based reductions for electrocatalytic $CO_2$ reduction in Scheme 1*B*. As dictated by the potentials for $Ru^{IV}=O^{2+} \rightarrow Ru^{V}=O^{3+}$ oxidation at approximately +1.55 V for peak a3 in Fig. 4*A*, which triggers water oxidation to $O_2$, and $[(tpy^-)(Mebim\text{-}py)Ru^{II}(CO_2{}^{2-})]^-$ reduction at approximately −1.45 V for peak b3 in Fig. 4*B*, which triggers $CO_2$ reduction to CO, $CO_2$ splitting in Eq. **7**, occurs at an applied cell potential of approximately 3.0 V [= + 1.55 − (−1.45)], with an overpotential of approximately 1.65 V (=3.0 − 1.35). The current densities of both anodic and cathodic scans in Fig. 4 are equivalent with overall cell performance limited by the rate of water oxidation at the anode as was determined by the separate studies on the half reactions in Figs. 1 and 2.

Fig. 5 shows a current-time (*i-t*) profile obtained by controlled potential electrolysis (3.0 V) under the conditions in Fig. 3 with two BDD|Si electrodes (approximately 0.85 $cm^2$). The physically separated gaseous products were collected in the head spaces of the separate electrode compartments for gas chromatographic analysis.

Based on the integrated *i-t* profiles in Fig. 5 and gas chromatographic analyses, coulombic efficiencies for formation of approximately 7.4 μmol of CO (approximately 5 TONs), approximately 0.5 μmol of $H_2$ (approximately 0.3 TONs), and approximately 2.9 μmol of $O_2$ (approximately 2 TONs) for a 3 h electrolysis period were approximately 76, 5, and 60%, respectively. CO and $O_2$ have a ratio of 2.5 : 1, close to the 2 : 1 expected for $CO_2$ split-

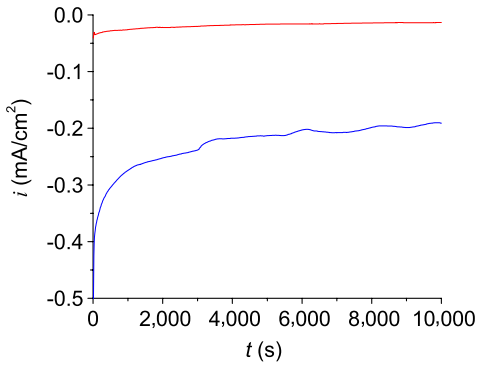


**Fig. 5.** Blue line: As in Fig. 3, controlled potential electrolysis at 3.0 V at two BDD|Si electrodes (approximately 0.85 $cm^2$). Red line: Background current without added catalyst. The solution was unstirred during the electrolysis to minimize solution equilibration between cell compartments.

[†]Note figure S8 in the Supporting Information in ref. 36 which documents slow loss of catalytic current as $HCO_3^-/CO_3^{2-}$ build up in solution leading to precipitation of the catalyst as the $HCO_3^-/CO_3^{2-}$ salt.

[‡]Nafion is slowly permeable to both water and $CH_3CN$. Based on a control experiment in an unstirred solution, solvent ($CH_3CN$-$H_2O$) inter-permeability across the Nafion|Frit separator in Fig. 3, was <2% in 24 h.

ting. For comparison, electrolysis under identical conditions but without catalyst resulted in <5% gaseous products.

The results described here illustrate the use of a single catalyst for $CO_2$ splitting, but this is only a first step. Under our conditions, electrocatalysis is limited by the rate of water oxidation at the anode. Long-term performance is further limited by slow carbene ligand oxidation at the anode* and catalyst precipitation at the cathode.† More efficient designs, based on ligand variations and surface attachment, are currently under investigation.

In its simplicity, the contrast with natural photosynthesis is striking. Photosynthesis in green plants involves thousands of atoms, five membrane-bound integrated assemblies, and the Calvin cycle and evolved over billions of years to achieve $CO_2$ splitting into oxygen and carbohydrates. In the electrochemical/photoelectrochemical approach, single catalysts or pairs of catalysts are combined with semiconductors, electrodes, wires, and membranes to connect the half reactions and exchange electrons and protons.

## Materials and Methods

**Chemicals.** $NaH_2PO_4$ (≥99.5%), $Na_2HPO_4$ (≥99.5%), and tetrabutylammonium hexafluorophosphate ($^nBu_4NPF_6$) was obtained from Fluka. $CO_2$ gas was purchased from Airgas National Welders (medical grade, 99.999%). All other reagents were ACS grade and used as received. All aqueous solutions were prepared with Milli-Q ultrapure water (>18 MΩ), and all nonaqueous solutions were prepared with acetonitrile ($CH_3CN$) of HPLC grade unless stated otherwise.

**Instrumentation.** Electrochemical measurements were performed with the model CHI660D electrochemical workstation. The three-electrode system for half-reaction study consisted of a working electrode, a platinum wire counter electrode, and a saturated calomel electrode (SCE) reference electrode (approximately 0.244 V vs. NHE) in aqueous solution or an $Ag/AgNO_3$ reference electrode (approximately 0.55 V vs. NHE) in nonaqueous solution. The two-electrode system for $CO_2$ splitting consisted of electrodes of the same materials, with one as the working electrode and the other acting as both counter and reference electrodes. In the two-electrode system, a second potentiostat was integrated to monitor the real potential applied at the working electrode by including an additional counter (Pt wire) and reference (SCE for aqueous solution or $Ag/AgNO_3$ for nonaqueous solution) electrodes to constitute a three-electrode system. Unless stated otherwise, all potentials were reported vs. NHE.

The gas product analysis in the headspace was conducted by gas chromatography (Varian 450-GC, molecular sieve column) with thermal-conductivity detector (TCD) for the detection of $O_2$ in the anode compartment and pulsed discharge helium ionization detector (PDHID) for the detection of CO and $H_2$ in the cathode compartment. Calibration curves for $O_2$, CO, and $H_2$ were determined separately. HC(O)H or $CH_3OH$ as possible products in the liquid phase were analyzed by gas chromatography with flame ionization detector (FID) (Shimadzu GC-2014, Agilent DB-Wax column) and $HC(O)O^-$ by $^1H$ NMR (Bruker Avance-400 MHz). For the latter, 30–50% $CD_3CN$ was added to the electrolyzed solution prior to NMR measurement. All experiments were performed at room temperature 22 °C.

**Synthesis.** Synthesis of catalyst **1** was reported elsewhere (38). Briefly, it was obtained by reaction of the monocationic carbene precursor ligand with $Ru(tpy)Cl_3$ in ethylene glycol at 150 °C in the presence of $NEt_3$. In this case, the aqua complex is the product rather than the chloro analog due to the *trans*-labilizing effect of the carbene.

**Other Procedures.** Prior to the experiments, the glassy carbon disk electrode (0.071 $cm^2$) was polished with 0.05 μm $Al_2O_3$ slurry to obtain a mirror surface followed by sonication in distilled water for 30 s to remove debris, and were thoroughly rinsed with Milli-Q ultrapure water.

The BDD|Si electrode (approximately 0.85 $cm^2$) was fabricated by depositing boron-doped diamond films on polycrystalline silicon wafers by microwave plasma-enhanced chemical vapor deposition (MPCVD). The MPCVD was performed in a 915 MHz plasma at a growth pressure of approximately 80 Torr. A 3% methane/hydrogen source gas, doped with 100 ppm of diborane, was used during deposition at a temperature of approximately 800 °C. The films were approximately 1.56 microns in thickness, with a sheet resistance of approximately 110 Ω/sq. The BDD|Si electrode was used for electrolysis without further treatment.

The glass frit-supported Nafion film (Nafion|Frit) was prepared by carefully spreading 40 μL of 2 wt % Nafion perfluorinated ion-exchange resin solution (diluted by methyl alcohol) onto the frit surface on the anode side (Fig. 3), followed by drying at room temperature.

**ACKNOWLEDGMENTS.** We thank Professor John Newman (University of California, Berkeley, CA) for helpful comments on the paper and Dr. Brian R. Stoner (RTI International, NC) for generous donation of BDD|Si slides. This work was supported by the University of North Carolina Energy Frontier Research Center (EFRC): Center for Solar Fuels an EFRC funded by the Department of Energy (DOE), Office of Science, Office of Basic Energy Sciences (BES), under Award DE-SC0001011 (to J.J.C., M.K.B., P.K., M.R.N., and P.G.H.). Support of electrochemical experiments by Z.-F.C. was provided by the same DOE BES EFRC Award DE-SC0001011. Support of product analysis by Z.-F.C. was provided by the Army Research Office through Grant W911NF-09-1-0426.

1. Meyer TJ, Papanikolas JM, Heyer CM (2011) Solar fuels and next generation photovoltaics: The UNC-CH energy frontier research center. *Catal Lett* 141:1–7.
2. Alstrum-Acevedo JH, Brennaman MK, Meyer TJ (2005) Chemical approaches to artificial photosynthesis. 2. *Inorg Chem* 44:6802–6827.
3. Gust D, Moore TA, Moore AL (2001) Mimicking photosynthetic solar energy transduction. *Acc Chem Res* 34:40–48.
4. Barber J (2009) Photosynthetic energy conversion: Natural and artificial. *Chem Soc Rev* 38:185–196.
5. Meyer TJ, Huynh MHV, Thorp HH (2007) The possible role of proton-coupled electron transfer (PCET) in water oxidation by photosystem II. *Angew Chem Int Ed* 46:5284–5304.
6. Nelson N, Yocum CF (2006) Structure and function of photosystems I and II. *Annu Rev Plant Biol* 57:521–565.
7. Nelson N, Ben-Shem A (2004) The complex architecture of oxygenic photosynthesis. *Nat Rev Mol Cell Biol* 5:971–982.
8. Kintisch E (2008) The greening of synfuels. *Science* 320:306–308.
9. Takeshita T, Yamaji K (2008) Important roles of Fischer-Tropsch synfuels in the global energy future. *Energy Policy* 36:2773–2784.
10. Huynh MHV, Meyer TJ (2007) Proton-coupled electron transfer. *Chem Rev* 107:5004–5064.
11. Costentin C, Robert M, Savéant JM (2010) Concerted proton-electron transfers: Electrochemical and related approaches. *Acc Chem Res* 43:1019–1029.
12. Hammes-Schiffer S (2009) Theory of proton-coupled electron transfer in energy conversion processes. *Acc Chem Res* 42:1881–1889.
13. McDaniel ND, Coughlin FJ, Tinker LL, Bernhard S (2008) Cyclometalated iridium(III) aquo complexes: Efficient and tunable catalysts for the homogeneous oxidation of water. *J Am Chem Soc* 130:210–217.
14. Tseng HW, Zong R, Muckerman JT, Thummel R (2008) Mononuclear ruthenium(II) complexes that catalyze water oxidation. *Inorg Chem* 47:11763–11773.
15. Hull JF, et al. (2009) Highly active and robust Cp* iridium complexes for catalytic water oxidation. *J Am Chem Soc* 131:8730–8731.
16. Gao Y, Akermark T, Liu JH, Sun LC, Akermark B (2009) Nucleophilic attack of hydroxide on a $Mn^V$ oxo complex: A model of the O–O bond formation in the oxygen evolving complex of photosystem II. *J Am Chem Soc* 131:8726–8727.
17. Romain S, Vigara L, Llobet A (2009) Oxygen–oxygen bond formation pathways promoted by ruthenium complexes. *Acc Chem Res* 42:1944–1953.
18. Wasylenko DJ, et al. (2010) Electronic modification of the $[Ru^{II}(tpy)(bpy)(OH_2)]^{2+}$ scaffold: Effects on catalytic water oxidation. *J Am Chem Soc* 132:16094–16106.
19. Grotjahn DB, et al. (2011) Evolution of iridium-based molecular catalysts during water oxidation with ceric ammonium nitrate. *J Am Chem Soc* 133:19024–19027.
20. Concepcion JJ, Jurss JW, Templeton JL, Meyer TJ (2008) One site is enough. Catalytic water oxidation by $[Ru(tpy)(bpm)(OH_2)]^{2+}$ and $[Ru(tpy)(bpz)(OH_2)]^{2+}$. *J Am Chem Soc* 130:16462–16463.
21. Concepcion JJ, Tsai MK, Muckerman JT, Meyer TJ (2010) Mechanism of water oxidation by single-site ruthenium complex catalysts. *J Am Chem Soc* 132:1545–1557.
22. Concepcion JJ, et al. (2009) Making oxygen with ruthenium complexes. *Acc Chem Res* 42:1954–1965.
23. Chen ZF, Concepcion JJ, Jurss JW, Meyer TJ (2009) Single-site, catalytic water oxidation on oxide surfaces. *J Am Chem Soc* 131:15580–15581.
24. Chen ZF, et al. (2010) Concerted O atom-proton transfer in the O–O bond forming step in water oxidation. *Proc Natl Acad Sci USA* 107:7225–7229.
25. Chen ZF, Concepcion JJ, Meyer TJ (2011) Rapid catalytic water oxidation by a single site, Ru carbene catalyst. *Dalton Trans* 40:3789–3792.
26. Takeda H, Ishitani O (2010) Development of efficient photocatalytic systems for $CO_2$ reduction using mononuclear and multinuclear metal complexes based on mechanistic studies. *Coord Chem Rev* 254:346–354.
27. Dubois MR, Dubois DL (2009) Development of molecular electrocatalysts for $CO_2$ reduction and $H_2$ production/oxidation. *Acc Chem Res* 42:1974–1982.
28. Morris AJ, Meyer GJ, Fujita E (2009) Molecular approaches to the photocatalytic reduction of carbon dioxide for solar fuels. *Acc Chem Res* 42:1983–1994.
29. Benson EE, Kubiak CP, Sathrum AJ, Smieja JM (2009) Electrocatalytic and homogeneous approaches to conversion of $CO_2$ to liquid fuels. *Chem Soc Rev* 38:89–99.

30. Nagao H, Mizukawa T, Tanaka K (1994) Carbon–carbon bond formation in the electrochemical reduction of carbon dioxide catalyzed by a ruthenium complex. *Inorg Chem* 33:3415–3420.
31. Smieja JM, Kubiak CP (2010) Re(bipy-tBu)$(CO)_3$Cl-improved catalytic activity for reduction of carbon dioxide: IR-spectroelectrochemical and mechanistic studies. *Inorg Chem* 49:9283–9289.
32. Radosevich AT, et al. (2009) Ligand reactivity in diarylamido/bis(phosphine) PNP complexes of Mn$(CO)_3$ and Re$(CO)_3$. *Inorg Chem* 48:9214–9221.
33. Pugh JR, Bruce MRM, Sullivan BP, Meyer TJ (1991) Formation of a metal-hydride bond and the insertion of carbon dioxide: Key steps in the electrocatalytic reduction of carbon dioxide to formate anion. *Inorg Chem* 30:86–91.
34. Bruce MRM, et al. (1992) Electrocatalytic reduction of carbon dioxide based on 2,2′-bipyridyl complexes of osmium. *Inorg Chem* 31:4864–4873.
35. Bolinger CM, Story N, Sullivan BP, Meyer TJ (1988) Electrocatalytic reduction of carbon dioxide by 2,2′-bipyridine complexes of rhodium and iridium. *Inorg Chem* 27:4582–4587.
36. Chen ZF, et al. (2011) Electrocatalytic reduction of $CO_2$ to CO by polypyridyl ruthenium complexes. *Chem Commun* 47:12607–12609.
37. Mauritz KA, Moore RB (2004) State of understanding of Nafion. *Chem Rev* 104:4535–4585.
38. Concepcion JJ, et al. (2009) Catalytic water oxidation by single-site ruthenium catalysts. *Inorg Chem* 49:1277–1279.